Modeling incompressible thermal flows using a central-moments-based lattice Boltzmann method

Linlin Fei [a], Kai Hong Luo [a,b,*], Chuandong Lin [a], Qing Li [c]

[a] Center for Combustion Energy, Key laboratory for Thermal Science and Power Engineering of Ministry of Education, Department of Energy and Power Engineering, Tsinghua University, Beijing 100084, China
[b] Department of Mechanical Engineering, University College London, Torrington Place, London WC1E 7JE, UK
[c] School of Energy Science and Engineering, Central South University, Changsha 410083, China

ABSTRACT

In this paper, a central-moments-based lattice Boltzmann method (CLBM) for incompressible thermal flows is proposed. In the method, the incompressible Navier-Stokes equations and the convection-diffusion equation for the temperature field are solved separately by two different CLB equations. Through the Chapman-Enskog analysis, the macroscopic governing equations for incompressible thermal flows can be reproduced. The consistent forcing scheme (Fei and Luo, 2017) is adopted to incorporate forcing effect, and the implementation for CLBM is simplified by using simplified raw-moment sets. Compared with several D2Q5 multiple-relaxation-time (MRT) lattice Boltzmann methods for the temperature equation, the proposed method is shown to be better Galilean invariant through measuring the thermal diffusivities on a moving reference frame. Numerical simulations for several typical problems confirm the accuracy, efficiency, and stability of the present method. The grid convergence tests indicate that the proposed CLBM for incompressible thermal flows is of second-order accuracy in space.

© 2017 The Authors. Published by Elsevier Ltd. This is an open access article under the CC BY license (http://creativecommons.org/licenses/by/4.0/).

1. Introduction

As a mesoscopic numerical method based on the kinetic theory, the lattice Boltzmann method (LBM) [1,2] has obtained remarkable success in the applications to fluid flows and heat transfer problems during the past three decades [3–7]. The LBM solves a discrete Boltzmann equation, designed to recover the Navier-Stokes (N-S) equations in the macroscopic limit. The highly efficient and easy algorithm of LBM makes it at affordable computational cost, while the mesoscale nature allows its natural incorporation of microscale and/or mesoscale physics [5].

In the standard collision-streaming algorithm for LBM, the simplest collision operator is the single-relaxation-time (SRT) or BGK operator, in which all the distribution functions are relaxed to their local equilibrium values at an identical rate [1]. However, the BGK-LBM may meet troubles of inaccuracy in implementing the boundary conditions [8,9], as well as numerical instability at high Reynolds number or low-viscosity flows [10,11]. Different from the BGK operator, the collision step in the multiple-relaxation-time (MRT) operator [10,11] is carried out in the raw-moment space. Compared with the BGK-LBM, the MRT-LBM can enhance numerical stability by carefully separating the time scales among the kinetic modes [11,12], as well as improve the numerical accuracy for non-slip boundary conditions by choosing a so-called "magic" parameter [8,9]. However, the MRT-LBM introduces non-Galilean artifact at non-unity Prandtl numbers in thermal lattice Boltzmann models [13]. In 2006, a cascaded operator was proposed by Geier et al. [14]. In the cascaded operator, the collision is carried out in the central-moment space, thus it is gradually interpreted as "central-moments-based" operator [15–17]. The central-moments-based LBM (CLBM) can enhance the numerical stability significantly compared to the BGK-LBM [14,15,17–19], which is also essentially due to the removal of the "ghost modes" [20]. Besides, Geier et al. argued that the collision in the central-moment space shows some advantages over the MRT operator in terms of numerical stability and Galilean invariance [14]. More comparisons and discussions between MRT and central-moments-based operators can be found in [13,14,21].

Recently, CLBM has been extended to multiphase flows by Lycett-Brown and Luo [18]. Compared with the BGK-LBM for

---

* Corresponding author at: Department of Mechanical Engineering, University College London, Torrington Place, London WC1E 7JE, UK.
  E-mail address: K.Luo@ucl.ac.uk (K.H. Luo).

multiphase flows, the proposed multiphase CLBM enables significant improvement in reducing spurious currents near the phase interface [18], and achieving higher stability range for the Reynolds number [19]. They further extended the model with an improved forcing scheme and made a breakthrough for large density ratio multiphase flow with high Reynolds and Weber numbers simultaneously [22]. In addition, CLBM has also been extended to simulate shallow water equations [23] and to simulate stationary flows coupled with a preconditioned method [24]. To incorporate forcing effect into CLBM, Premnath et al. proposed a forcing scheme by method of central moments [25]. In Ref. [18], Lycett-Brown and Luo adopted the forcing scheme for the BGK-LBM in the CLBM directly. De Rosis also proposed alternative formulations to incorporate forcing terms [16,26]. Based on a general multiple-relaxation-time (MRT) framework, a consistent forcing scheme in CLBM was recently proposed by the present authors [27]. The proposed consistent forcing scheme shows great advantages over several previous forcing schemes in terms of consistency, accuracy, and isotropy. More recently, a thermal cascaded LBM (TCLBM) has been proposed by the present authors to simulate low-Mach compressible thermal flows [28]. The TCLBM was based on the double-distribution-function (DDF) approach, which is a widely used method for constructing thermal LBMs in the LBM community [6,29–32]. Shah et al. proposed another DDF-based CLBM to simulate fluid and heat transport in porous media [33], in which the D2Q9 density and temperature equilibrium functions were used, and the forcing effect was incorporated by a simple method. The model proposed by Shah et al. has been used to study convective heat transfer enhancement in jet impingement due to the presence of porous media [34]. Meanwhile, Sharma et al. proposed another DDF-based CLBM for convective heat transfer [35], where the D2Q5 model was used for the temperature field. In this paper, we propose a new CLBM for incompressible thermal flows based on a general multiple-relaxation-time framework [27], which is different from the previous methods [28,33,35] in three respects: (1) the consistent forcing scheme [27] is used to incorporate forcing effect; (2) the equilibrium central moments for the temperature field are also given by the continuous central moments of a continuous "temperature" distribution [see in Eq. (22)]; (3) simplified raw moment sets are adopted for both the density and the temperature distributions [see in Eqs. (6) and (16)].

The rest of the paper is structured as follows: In Section 2, the two-dimensional (2D) CLBM for incompressible thermal flows is presented. Numerical experiments are carried out for several benchmark problems to validate the proposed method in Section 3. Finally, concluding remarks are given in Section 4.

2. CLBM for incompressible thermal flows

In this section, the construction of the CLBM for incompressible thermal flows is present. The macroscopic governing equations for the flow fields are

$$\nabla \cdot \mathbf{u} = 0, \tag{1a}$$

$$\frac{\partial \mathbf{u}}{\partial t} + \mathbf{u} \cdot \nabla \mathbf{u} = -\frac{1}{\rho_0} \nabla p + \nu \nabla^2 \mathbf{u} + \mathbf{F}, \tag{1b}$$

where $\mathbf{u}, p, \rho_0, \mathbf{F}$ and ν are the velocity, pressure, reference density, force field and kinematic viscosity, respectively. The convection-diffusion equation for a scalar variable ϕ with diffusion coefficient D can be written as

$$\frac{\partial \phi}{\partial t} + \mathbf{u} \cdot \nabla \phi = \nabla \cdot (D \nabla \phi). \tag{2}$$

For incompressible thermal flows considered in this study, the scalar variable and diffusion coefficient are specified as temperature T and thermal diffusivity α, respectively. To include the effect of temperature field on the flow field, the Boussinesq assumption is used and the force field is defined by

$$\mathbf{F} = -g\beta(T - T_0)\mathbf{j} + \mathbf{F}_\nu, \tag{3}$$

where g is the magnitude of gravitational acceleration, β is the thermal expansion coefficient, $\mathbf{j}$ is the unit vector in the vertical direction, T_0 is the reference temperature, and $\mathbf{F}_\nu$ is an external body force.

2.1. CLBM for the flow field

The two-dimensional (2D) problems are considered in this study, and the D2Q9 lattice [1] is used for the flow field. The lattice speed $c = \Delta x / \Delta t = 1$ is adopted, where Δx and Δt are the lattice space and time steps. The discrete velocities $\mathbf{e}_i = [|e_{ix}\rangle, |e_{iy}\rangle]$ are defined by

$$|e_{ix}\rangle = [0, 1, 0, -1, 0, 1, -1, -1, 1]^\top, \tag{4a}$$

$$|e_{iy}\rangle = [0, 0, 1, 0, -1, 1, 1, -1, -1]^\top, \tag{4b}$$

where $i = 0 \ldots 8, |\cdot\rangle$ denotes the column vector, and the superscript $\top$ denotes the transposition.

To construct the central-moments-based collision operator, raw moments and central moments for the discrete distribution functions (DFs) f_i are introduced [14],

$$k_{mn} = \left\langle f_i \middle| e_{ix}^m e_{iy}^n \right\rangle, \tag{5a}$$

$$\tilde{k}_{mn} = \left\langle f_i \middle| (e_{ix} - u_x)^m (e_{iy} - u_y)^n \right\rangle, \tag{5b}$$

and the equilibrium values k_{mn}^{eq} and $\tilde{k}_{mn}^{eq}$ are defined analogously by replacing f_i with the discrete equilibrium distribution functions (EDFs) f_i^{eq}. In the literature, many researchers [14,16,26,18,19,23,24,22,25,27,28,33,35] adopted the recombined raw moments, $k_{20} + k_{02}$ and $k_{20} - k_{02}$, to treat the trace of the pressure tensor and the normal stress difference independently, while the practical implementation is tedious, especially for three-dimensional (3D) models. To simplify the practical implementation, a simplified method was proposed in [36], where the raw moments, k_{20} and k_{02}, were used and some modifications were made in the relaxation matrix. In this work, the simplified raw-moment set is adopted,

$$|\Gamma_i\rangle = [k_{00}, k_{10}, k_{01}, k_{20}, k_{02}, k_{11}, k_{21}, k_{12}, k_{22}]^\top, \tag{6}$$

and so do the recombined central moments $\tilde{\Gamma}_i$. To be more specific, the raw moments are transformed from f_i through a transformation matrix $\mathbf{M}$ by $|\Gamma_i\rangle = \mathbf{M}|f_i\rangle$, and the central moments are shifted from raw moments through a shift matrix $\mathbf{N}$ by $\left|\tilde{\Gamma}_i\right\rangle = \mathbf{N}|\Gamma_i\rangle$ [27,36]. The expressions for $\mathbf{M}$ and $\mathbf{N}$ are written as,

$$\mathbf{M} = \begin{bmatrix} 1 & 1 & 1 & 1 & 1 & 1 & 1 & 1 & 1 \\ 0 & 1 & 0 & -1 & 0 & 1 & -1 & -1 & 1 \\ 0 & 0 & 1 & 0 & -1 & 1 & 1 & -1 & -1 \\ 0 & 1 & 0 & 1 & 0 & 1 & 1 & 1 & 1 \\ 0 & 0 & 1 & 0 & 1 & 1 & 1 & 1 & 1 \\ 0 & 0 & 0 & 0 & 0 & 1 & -1 & 1 & -1 \\ 0 & 0 & 0 & 0 & 0 & 1 & 1 & -1 & -1 \\ 0 & 0 & 0 & 0 & 0 & 1 & -1 & -1 & 1 \\ 0 & 0 & 0 & 0 & 0 & 1 & 1 & 1 & 1 \end{bmatrix}, \tag{7a}$$

$$\mathbf{N} = \begin{bmatrix} 1 & 0 & 0 & 0 & 0 & 0 & 0 & 0 & 0 \\ -u_x & 1 & 0 & 0 & 0 & 0 & 0 & 0 & 0 \\ -u_y & 0 & 1 & 0 & 0 & 0 & 0 & 0 & 0 \\ u_x^2 & -2u_x & 0 & 1 & 0 & 0 & 0 & 0 & 0 \\ u_y^2 & 0 & -2u_y & 0 & 1 & 0 & 0 & 0 & 0 \\ u_x u_y & -u_y & -u_x & 0 & 0 & 1 & 0 & 0 & 0 \\ -u_x^2 u_y & 2u_x u_y & u_x^2 & -u_y & 0 & -2u_x & 1 & 0 & 0 \\ -u_y^2 u_x & u_y^2 & 2u_x u_y & 0 & -u_x & -2u_y & 0 & 1 & 0 \\ u_x^2 u_y^2 & -2u_x u_y^2 & -2u_y u_x^2 & u_y^2 & u_x^2 & 4u_x u_y & -2u_y & -2u_x & 1 \end{bmatrix}. \tag{7b}$$

Compared with the expressions for $\mathbf{M}$ and $\mathbf{N}$ in [27], the expressions here are simpler and can reduce the computational cost, and this effect could be much more evident for 3D models.

By relaxing each central moment to its equilibrium counterpart independently, the post-collision central moments are given by

$$\left|\tilde{\Gamma}_i^*\right\rangle = (\mathbf{I} - \mathbf{S})\left|\tilde{\Gamma}_i\right\rangle + \mathbf{S}\left|\tilde{\Gamma}_i^{eq}\right\rangle + (\mathbf{I} - \mathbf{S}/2)|C_i\rangle, \tag{8}$$

where C_i are the forcing source terms in central moment space, and the block-diagonal relation matrix is given by,

$$\mathbf{S} = diag\left([s_0, s_1, s_1], \begin{bmatrix} s_+, s_- \\ s_-, s_+ \end{bmatrix}, [s_v, s_3, s_3, s_4]\right), \tag{9}$$

with $s_+ = (s_b + s_v)/2$ and $s_- = (s_b - s_v)/2$. The equilibrium central moments of f_i^{eq} are set equal to the continuous central moments of the Maxwellian-Boltzmann distribution in continuous velocity space [14,18,25],

$$\left|\tilde{\Gamma}_i^{eq}\right\rangle = [\rho, 0, 0, \rho c_s^2, \rho c_s^2, 0, 0, 0, \rho c_s^4]^\top, \tag{10}$$

where ρ is the fluid density, and $c_s = \sqrt{1/3}$ is the lattice sound speed. The corresponding EDF is in fact a generalized local equilibrium [25,36]. According to He et al. [37], the forcing terms in discrete velocity space are written as

$$R_i = \frac{\mathbf{F}}{\rho} \frac{(\mathbf{e}_i - \mathbf{u})}{c_s^2} f_i^{eq}. \tag{11}$$

Consistently, the forcing source terms in central-moment space are defined as [27],

$$|C_i\rangle = \mathbf{NM}|R_i\rangle = [0, F_x, F_y, 0, 0, 0, c_s^2 F_y, c_s^2 F_x, 0]^\top. \tag{12}$$

In the streaming step, the post-collision discrete DFs in space $\mathbf{x}$ stream to their neighbors $\mathbf{x} + \mathbf{e}_i\Delta t$ along the characteristic lines as usual

$$f_i(\mathbf{x} + \mathbf{e}_i\Delta t, t + \Delta t) = f_i^*(\mathbf{x}, t), \tag{13}$$

where the post-collision discrete DFs are determined by $|f_i^*\rangle = \mathbf{M}^{-1}\mathbf{N}^{-1}|\tilde{\Gamma}_i^*\rangle$. The hydrodynamics variables are obtained by,

$$\rho = \sum_{i=0}^8 f_i, \quad \rho\mathbf{u} = \sum_{i=0}^8 f_i\mathbf{e}_i + \Delta t\mathbf{F}/2. \tag{14}$$

In the present method, the incompressible approximation [38] is employed, i.e., $\rho = \rho_0 + \delta\rho$, and $\delta\rho$ is the density fluctuation. Using the Chapman-Enskog analysis, the incompressible N-S equation in Eq. (1) can be reproduced in the low-Mach number limit [25]. The kinematic and bulk viscosities are related to the relaxation parameters by $v = (1/s_v - 0.5)c_s^2\Delta t$ and $\xi = (1/s_b - 0.5)c_s^2\Delta t$, respectively.

2.2. CLBM for the temperature field

In this subsection, a new D2Q5 (the five discrete velocity set is defined in Eq. (4), $\{\mathbf{e}_i = [|e_{ix}\rangle, |e_{iy}\rangle]|i = 0, 1, \dots 4\}$) CLBM is proposed to solve the convection-diffusion equation for the temperature field. Similarly, the raw moments and central moments of the temperature distribution functions g_i can be defined by

$$k_{mn}^T = \left\langle g_i \middle| e_{ix}^m e_{iy}^n \right\rangle, \tag{15a}$$

$$\tilde{k}_{mn}^T = \langle g_i | (e_{ix} - u_x)^m (e_{iy} - u_y)^n \rangle. \tag{15b}$$

In the D2Q5 lattice, the simplified raw-moment set is also used (rather than the recombined raw-moment set $\left|\Gamma_i^T\right\rangle = \left[k_{00}^T, k_{10}^T, k_{01}^T, k_{20+02}^T, k_{02-20}^T\right]^\top$ used in [35]),

$$\left|\Gamma_i^T\right\rangle = \left[k_{00}^T, k_{10}^T, k_{01}^T, k_{20}^T, k_{02}^T\right]^\top, \tag{16}$$

and so do the recombined central moments $\left|\tilde{\Gamma}_i^T\right\rangle$. Analogously, the raw moments and central moments can be calculated through a transformation matrix $\mathbf{M}_T$ and a shift matrix $\mathbf{N}_T$, respectively

$$\left|\Gamma_i^T\right\rangle = \mathbf{M}_T|g_i\rangle, \quad \left|\tilde{\Gamma}_i^T\right\rangle = \mathbf{N}_T\left|\Gamma_i^T\right\rangle. \tag{17}$$

Explicitly, $\mathbf{M}_T$ and $\mathbf{N}_T$ are expressed as

$$\mathbf{M}_T = \begin{bmatrix} 1 & 1 & 1 & 1 & 1 \\ 0 & 1 & 0 & -1 & 0 \\ 0 & 0 & 1 & 0 & -1 \\ 0 & 1 & 0 & 1 & 0 \\ 0 & 0 & 1 & 0 & 1 \end{bmatrix}, \tag{18a}$$

$$\mathbf{N}_T = \begin{bmatrix} 1 & 0 & 0 & 0 & 0 \\ -u_x & 1 & 0 & 0 & 0 \\ -u_y & 0 & 1 & 0 & 0 \\ u_x^2 & -2u_x & 0 & 1 & 0 \\ u_y^2 & 0 & -2u_y & 0 & 1 \end{bmatrix}. \tag{18b}$$

The collision in central moments can also be written as

$$\left|\tilde{\Gamma}_i^{T,*}\right\rangle = (\mathbf{I} - \mathbf{S}_T)\left|\tilde{\Gamma}_i^T\right\rangle + \mathbf{S}_T\left|\tilde{\Gamma}_i^{T,eq}\right\rangle, \tag{19}$$

where $\mathbf{S}^T = diag(\lambda_o, \lambda_1, \lambda_1, \lambda_2, \lambda_2)$ is the diagonal relaxation matrix. Similar to the Maxwell-Boltzmann distribution, we define a continuous "temperature" equilibrium distribution in the continuous velocity space (ξ_x, ξ_y),

$$g^{eq} = \frac{T}{2\pi c_T^2} \exp\left[-\frac{(\xi - \mathbf{u})^2}{2c_T^2}\right], \tag{20}$$

where c_T is the "sound speed". Then we take the important step by equating discrete central moments of g_i^{eq} to the continuous central moments of g^{eq},

$$\langle g_i^{eq} | (e_{ix} - u_x)^m (e_{iy} - u_y)^n \rangle = \int_{-\infty}^\infty \int_{-\infty}^\infty g^{eq} (\xi_x - u_x)^m (\xi_y - u_y)^n d\xi_x d\xi_y. \tag{21}$$

Thus the equilibrium values of $\tilde{\Gamma}_i^T$ can be written as

$$\left|\tilde{\Gamma}_i^{T,eq}\right\rangle = \left[T, 0, 0, Tc_T^2, Tc_T^2\right]^\top. \tag{22}$$

The post-collision temperature distribution functions g_i^* can be obtained by

$$g_i^* = \mathbf{M}_T^{-1}\mathbf{N}_T^{-1}\left|\tilde{\Gamma}_i^{T,*}\right\rangle. \qquad (23)$$

The streaming step for g_i^* also takes the form

$$g_i(\mathbf{x} + \mathbf{e}_i\Delta t, t + \Delta t) = g_i^*(\mathbf{x}, t). \qquad (24)$$

The temperature T is computed as

$$T = \sum_{i=0}^{4} g_i. \qquad (25)$$

As shown in Appendix A, the convection-diffusion Eq. (2) can be recovered by the above D2Q5 CLBM, and the thermal diffusivity is related to the relaxation parameter through $\alpha = (1/\lambda_1 - 0.5)c_T^2\Delta t$.

3. Numerical experiments

In this section, we conduct several benchmark cases to verify the effectiveness and accuracy of the proposed CLBM for incompressible thermal flows. Unless otherwise specified, the lattice sound speed for the D2Q5 CLBM is set to $c_T = \sqrt{1/2}$, the tunable relaxation parameters for high-order central moments are set to 1.0, and the non-equilibrium bounce-back method [39] and non-equilibrium extrapolation method [30] are adopted for velocity and temperature boundary conditions, respectively. It should be noted that the half-way bounce-back scheme has also been extended to implement general boundary conditions for the convection-diffusion equation and shows high accuracy and stability. More information on the boundary treatments can be found in [40,41] and the references cited therein.

3.1. The decay of a temperature wave

Firstly, the decay of a temperature wave on a moving frame is considered. The problem is specified by the following velocity and temperature fields:

$$\mathbf{u} = [0, A]. \qquad (26a)$$

$$T = T_0 + B\sin\left[\phi(y - At)\right]\exp(-\phi^2\alpha t). \qquad (26b)$$

where A represents the vertical reference velocity component, $B = 0.01$ is the initial amplitude of the temperature wave, $T_0 = 1.0$ is the reference temperature, $\phi = 2\pi/L$, and $L = 100$ is height of the computational domain. Periodic boundary conditions are used along the x and y axes. The velocity field is given, thus only the D2Q5 CLBM is adopted to solve the temperature field. Another two D2Q5 MRT LBMs in [32,41] are also used for comparison, and they are denoted by MRT-LBM1 and MRT-LBM2, respectively.

Firstly, the case at Mach number $Ma = A/c_s = 0.3$ is considered. The profiles for the dimensionless temperature T^* in different methods at the time $t^* = 2.0$ are shown in Fig. 1, where $T^* = (T - T_0)/B$ and $t^* = \phi^2\alpha t$. It is found that the simulation result of the present CLBM is in good agreement with the analytical solution, while there are visible differences between the numerical solutions by the other two methods and the analytical solution. The measured thermal diffusivity of the simulated fluid is obtained by measuring the time decay of the temperature wave. Then, the measured thermal diffusivities of each method at different Mach numbers are compared in Fig. 2, while the originally given thermal diffusivity is $\alpha = 0.05$. For the present D2Q5 CLBM, the measured thermal diffusivity is independent of the reference velocity (or Ma) and always agrees with the given value. For the other two D2Q5 MRT LBMs, the measured diffusivities decrease with the increase of the reference velocity. To be specific, the relative errors at $Ma = 0.3$ are around 12% and 8% for MRT-LBM1 and MRT-LBM2, respectively.
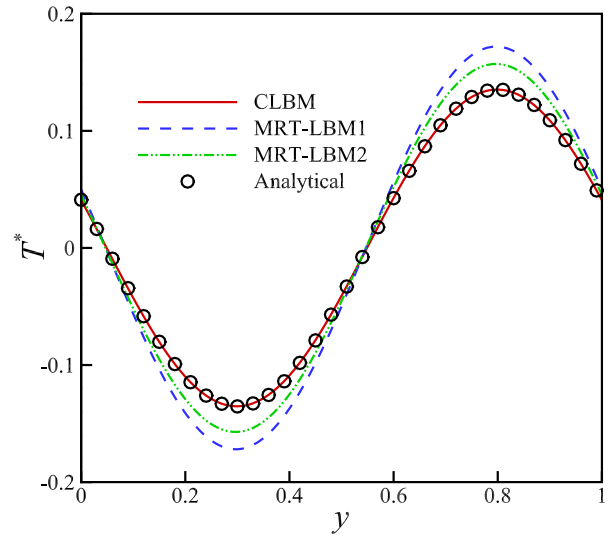

Fig. 1. Comparison of the temperature profiles at $t^* = 2.0$ simulated by different methods.
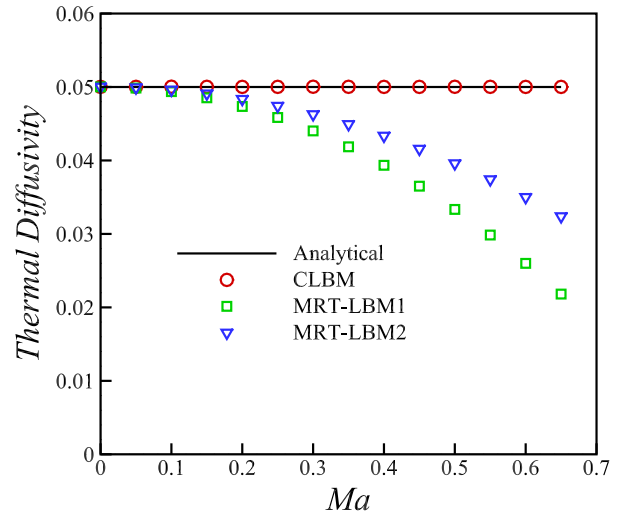

Fig. 2. Comparison of thermal diffusivities measured by each method at different values of Ma.

As shown in the above, the present method has better Galilean invariance compared with the two MRT methods. However, the mixed derivative terms still exist in the present method, and cannot be eliminated naturally due to the limit of the D2Q5 lattice (see in Appendix A). To restore the complete Galilean invariant, additional correction terms [42] or more symmetrical lattice, such as D2Q9 lattice, are needed.

3.2. Normal plate velocity problem with a temperature difference

The normal plate velocity problem is a fully developed channel flow, where the upper plate moves with a uniform velocity u_0, and a uniform normal flow with velocity v_0 is injected through the bottom plate and withdrawn from the upper plate. The analytical solution of the flow is given by [43],

$$\frac{u_a}{u_0} = \frac{\exp(Re \cdot y/L) - 1}{\exp(Re) - 1}, \qquad (27)$$

where the Reynolds number is based on the width of the channel, L, and defined by $Re = v_0L/v$. For the present study, a temperature

difference $\Delta T = T_H - T_L$ is considered, where T_H and T_L are the temperatures at upper hot plate and lower cold plate, respectively. The steady temperature profile satisfies [29],

$$\frac{T_a - T_L}{\Delta T} = \frac{\exp(RePr \cdot y/L) - 1}{\exp(RePr) - 1}, \tag{28}$$

where $Pr = \nu/\alpha$ is the Prandtl number.

In all the simulations, we set $T_H = 1.0, T_L = 0, \nu = 0.1$ and $u_0 = 0.02$. Firstly, we set the Reynolds number $Re = 10$, $\nu_0 = Re\nu/L$ with $L = 50$. Periodic boundary conditions are adopted at the inlet and outlet of channel, and the length of the channel is covered by 5 grids to save the computational cost. Three simulation cases with $Pr = [0.1, 1, 10]$ are conducted to verify the numerical performance of the present method at a wide range of the Prandtl number. As shown in Fig. 3, the numerical results for the non-dimensional temperature $T^* = (T - T_0)/\Delta T$ are in very good agreement with the analytical solutions.

Then we set the Prandtl number corresponding to air, $Pr = 0.71$, with different values of the Reynolds number, $Re = [10, 20, 30]$. The width of the channel is covered by a series of grid nodes, $L = [20, 40, 80, 160]$, to validate the convergence rate in space. The relative errors of temperature and velocity are calculated according to the following definitions,
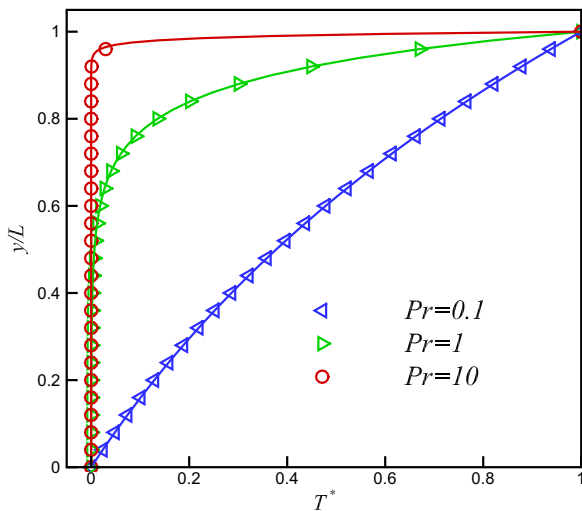
$$E_T = \sqrt{\frac{\sum (T - T_a)^2}{\sum T_a^2}}, \quad E_u = \sqrt{\frac{\sum (u - u_a)^2}{\sum u_a^2}}. \tag{29}$$

The relationships between grid sizes and relative errors of the present method are plotted in Fig. 4, and the slope of each fitting line is close to 2.0. This demonstrates that the method proposed is of second-order convergence rate in space.

3.3. Rayleigh-Bénard convection

In this section, the Rayleigh-Bénard convective flow is conducted to check the ability of simulating incompressible thermal flows with an external force field. In the 2D Rayleigh-Bénard convective flow, the fluid is enclosed between two parallel stationary walls, with high temperature T_H at the bottom and low temperature T_L at the top, and experiences the gravity. The gravity field is incorporated by Eq. (3).

The flow is characterized by the length-width ratio of the flow domain $L : H$, the Prandtl number $Pr = \nu/\alpha$ and Rayleigh number $Ra = g\beta\Delta TH^3/(\nu\alpha)$. In the simulations, we set $L \times H = 60 \times 30$, $Pr = 0.71, T_H = 1.05, T_L = 0.95$, and $T_0 = (T_H + T_L)/2 = 1.0$. The characteristic velocity of the convection is $u_c = \sqrt{g\beta\Delta TH}$, and the Mach number is defined as $Ma = u_c/c_s$. For a given Rayleigh number, the viscosity is calculated according to $\nu = Mac_sH\sqrt{Pr/Ra}$. To set up the simulation, an initial small disturbance is given to the density field along the horizontal center line,

$$\rho(x, H/2) = \rho_0[1.0 + 0.001\cos(2\pi x/L)], \tag{30}$$

while the densities at other points are initialized as ρ_0, and $\rho_0 = 1.0$.

The characteristic time of the system can be expressed by $t_c = H/u_c = Hc_s/Ma$. It is known that the iterations needed for the convergence are proportional to t_c. Firstly, we change Ma from 0.1 to 0.31 with a 0.03 interval, and calculate the needed time steps until convergence. From Fig. 5, we certainly confirm the linear relation between the needed time steps and $1/Ma$. Throughout the variation range of Ma, the relative changes of the Nusselt number (defined in Eq. (31)) are only 0.11%, 0.10% and 0.08% for the Rayleigh numbers at 2500, 3000, and 5000, respectively. We try to check the effectiveness and accuracy for a relatively high Ma at a wider range of Ra. In the following simulations, the Mach number is set to be $Ma = 0.3$. In addition, it should be noted that a preconditioned method can also be used to reduce the computational cost in CLBM [24].

Fig. 3. Comparison of numerical temperature profiles (symbols) and the analytical solutions (solid lines) at different values of the Pr.
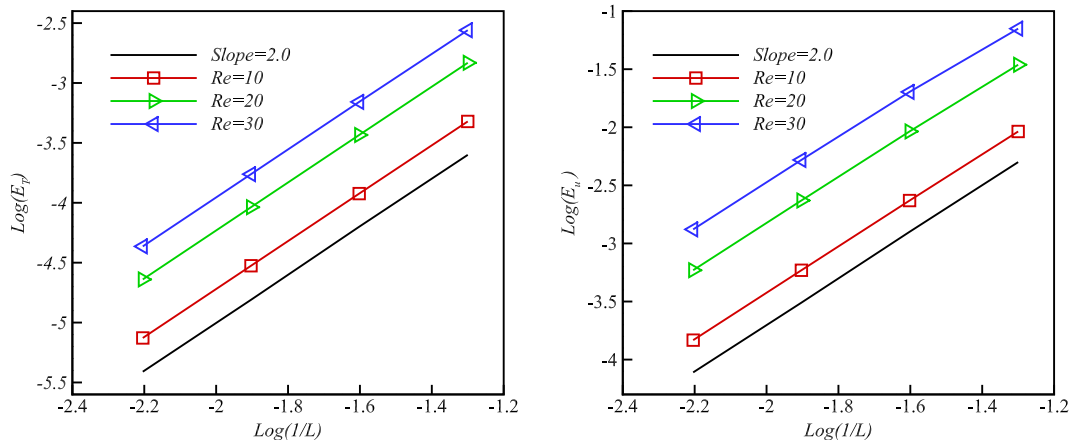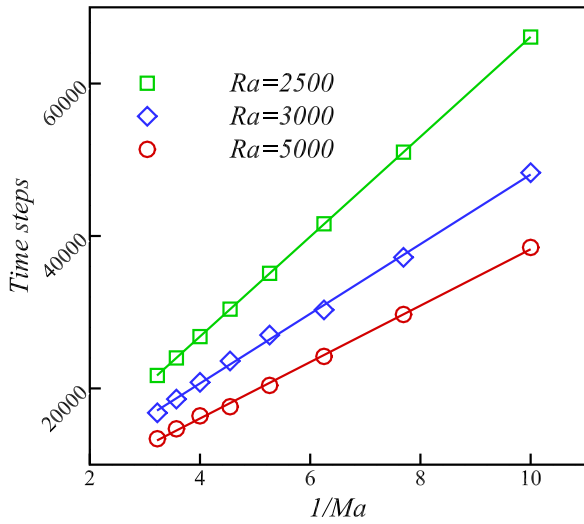
Fig. 4. Relative errors of temperature (left) and velocity (right) change with grid sizes at $Pr = 0.71$. The slopes of the fitting lines at $Re = [10, 20, 30]$ are [2.0013, 2.0025, 1.9988] (left) and [1.9895, 1.9601, 1.9364] (right), respectively.

Fig. 5. Time steps needed for convergence change with the reciprocal of *Ma*.

According to the linear stability theory, the driven force by the density variations induced by the temperature variations will be balanced by the viscous force when Rayleigh number is lower than a critical value Ra_c, while if the Rayleigh number is increased above the threshold, the driving force will dominate and convection will be induced. To determine the critical Rayleigh number, we measure the evolution of the maximal vertical velocity in the system V_{max} for a series of Rayleigh numbers, $Ra = [1702, 1704, 1706, 1708, 1710]$. It can be seen in Fig. 6 that V_{max} will keep increasing/decreasing approximately linearly in the early period, depending on Ra. The critical Rayleigh number is determined by solving zero value for the growth rate of V_{max} with the least-square method. Compared with the exact value in the linear stability theory, $Ra_c = 1707.76$, the value based on our method, 1706.82, is satisfying.

Flows at different Rayleigh numbers are then simulated. Fig. 7 displays the normalized temperature $(T - T_0)/\Delta T$ at $Ra = 2000$, 10,000 and 50000. When the Rayleigh number increases, we can see two clear trends in the figures: the mixing of the hot and cold
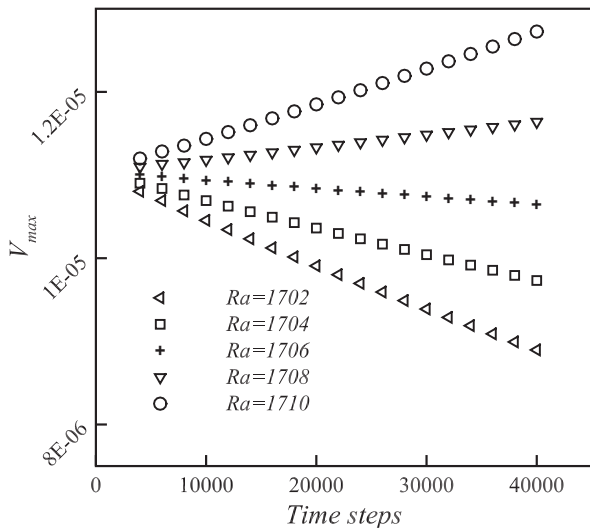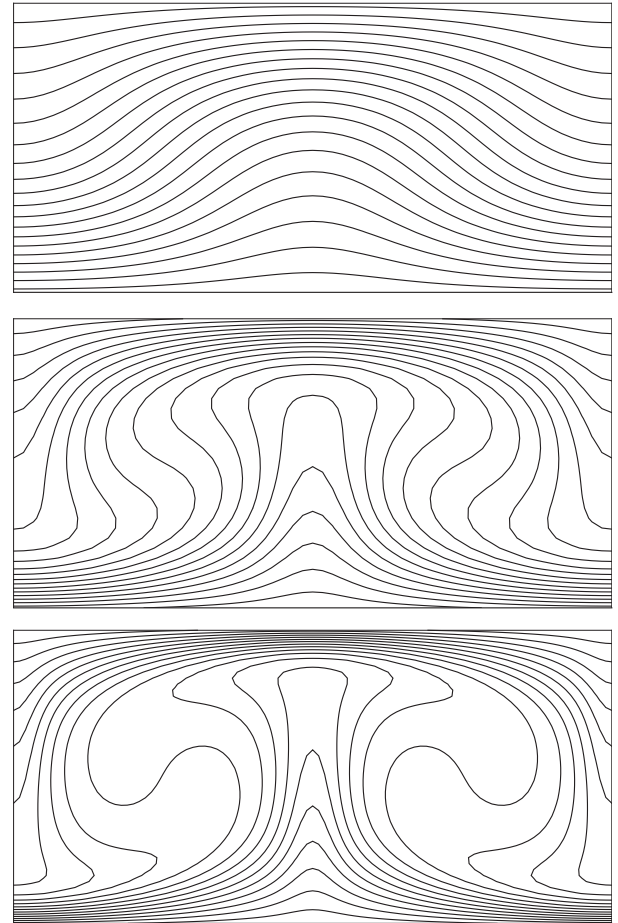

Fig. 7. Isotherms for Rayleigh-Bénard convective flows. From top to bottom, $Ra = 2000$, 10,000 and 50,000.

fluids is enhanced, and the temperature gradients near the bottom and top walls are increased, both of which mean the convective heat transfer is enhanced in the domain. In the meantime, as shown in Fig. 8, the vortex is gradually distorted with the increase of the Rayleigh number, which also means the enhancement of convection. To quantify this, the Nusselt number in the system is calculated [44],

$$Nu = 1 + \frac{\langle u_y T \rangle H}{\alpha \Delta T}, \tag{31}$$

where the square bracket represents the average over the whole system. Nusselt numbers obtained at various Rayleigh numbers are compared with the reference data in Table 1. The simulation results are in good agreement with the analytical values in [44]. On the whole, the relative errors for the present method are smaller than the method in [45], while only 60×30 nodes are used in the present method compared to 100×50 nodes in [45].

In the end, we illustrate the snapshot of the temperature field at $Ra = 10^9$ in Fig. 9. It is interesting to find that the proposed method is stable for Ra reaching up to 10^9 with only 220 nodes in the vertical direction. Hence, the commendable stability of the method is confirmed. As also shown in Appendix B, by comparing the achievable Re for the lid-driven cavity flow at the same mesh, it is demonstrated that CLBM improves the numerical stability significantly compared to the BGK-LBM. However, the study of *high-Ra* or *high-Re* thermal flows is beyond the scope of the current paper.
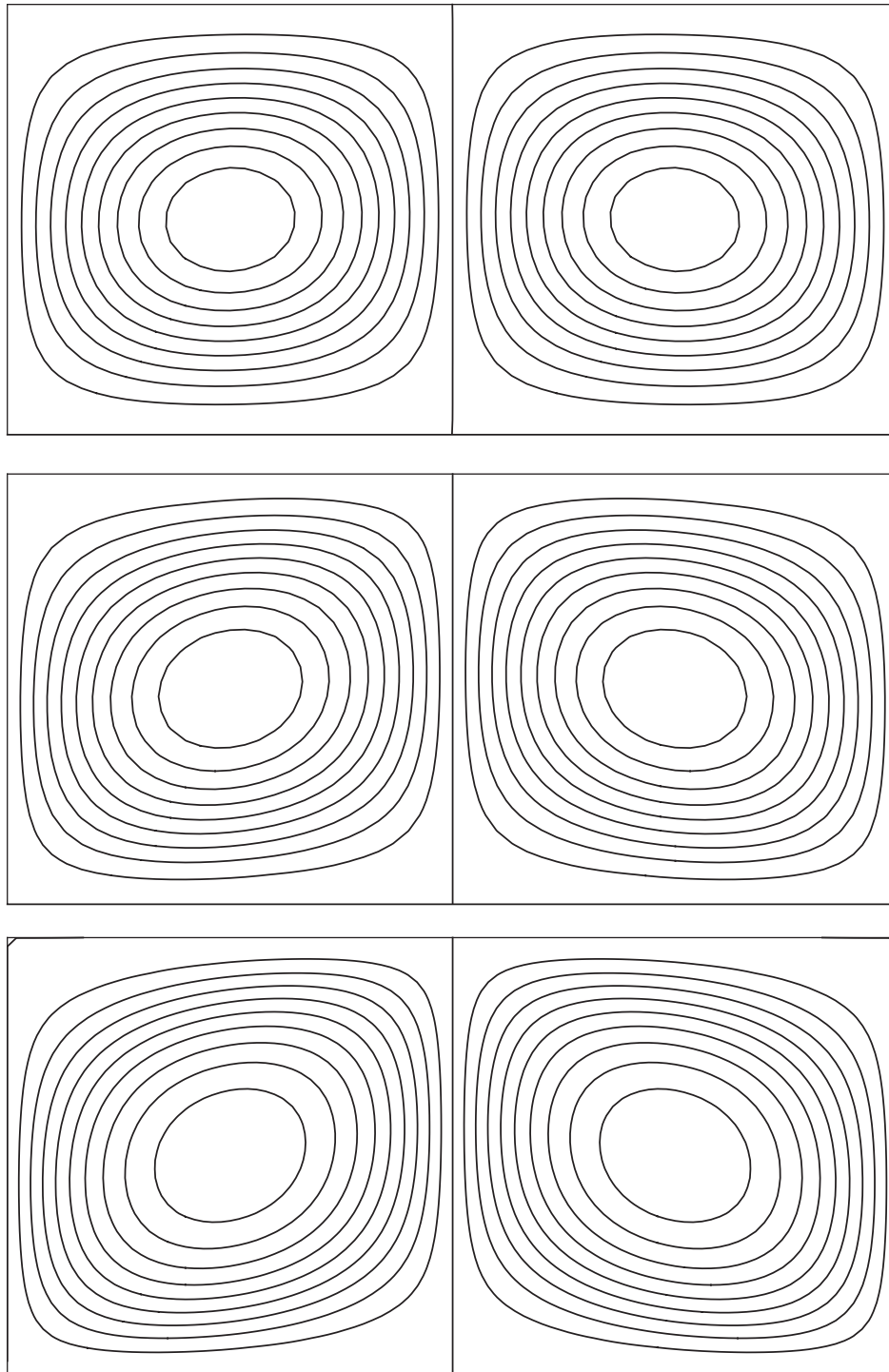

Fig. 6. The evolution of V_{max} with time at $Ra = [1702, 1704, 1706, 1708, 1710]$.

Fig. 8. Streamlines for Rayleigh-Bénard convective flows. From top to bottom, Ra = 2000, 10,000 and 50,000.

4. Conclusions

In this paper, we have developed a central-moments-based lattice Boltzmann method (CLBM) for incompressible thermal flows. Combined with the D2Q9 CLB equation for the flow field, another D2Q5 CLB equation is designed to reproduce the temperature equation. Through the Chapman-Enskog analysis, the macroscopic governing equations for incompressible thermal flows can be recovered. Compared with some existing thermal LBMs

[32,35,41], the proposed model achieves better Galilean invariance. Numerical simulations for several typical problems confirm the accuracy, efficiency, and stability of the present method. It is shown that a relatively high Mach number can be adopted in the present method for Rayleigh-Bénard convective flow (at $Ra \leqslant$ 50,000), thus the computational cost can be reduced significantly. The method developed retains the simplicity and numerical efficiency of the standard LBM. Furthermore, it is straightforward to extend this method to simulate 3D problems. Besides, the model

Table 1
Comparison of Nusselt number between the present numerical results and the results in Refs. [44,45].

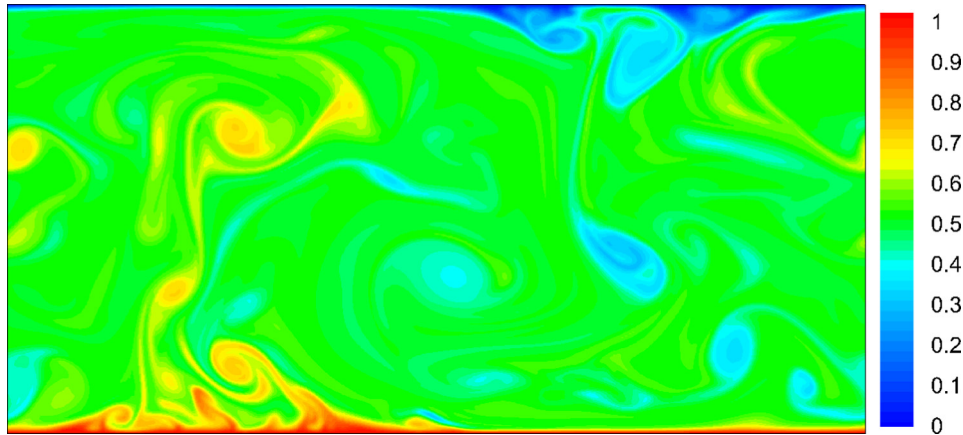| Cases	Analytic N_u [44]	Present method		Results in Ref. [45]	
		N_u	Relative error	N_u	Relative error
2000	1.212	1.213	0.08	–	–
2500	1.475	1.477	0.13	1.474	0.07
3000	1.663	1.667	0.24	–	–
5000	2.116	2.121	0.24	2.104	0.57
10,000	2.661	2.672	0.41	2.664	0.64
20,000	3.258	3.271	0.4	–	–
30,000	3.662	3.668	0.16	3.605	1.56
50,000	4.245	4.229	0.38	4.133	2.64

Fig. 9. Snapshot of the temperature field at $Ra = 10^9$.

developed can also be applied to other convection-diffusion problems directly.

Conflict of interest

None declared.

Acknowledgments

Appendix A. Chapman-Enskog analysis of the CLBM for temperature field

The explicit expressions for $\mathbf{M}_T^{-1}$ and $\mathbf{N}_T^{-1}$ are as follows.

$$\mathbf{M}_T^{-1} = \begin{bmatrix} 1 & 0 & 0 & -1 & -1 \\ 0 & 1/2 & 0 & 1/2 & 0 \\ 0 & 0 & 1/2 & 0 & 1/2 \\ 0 & -1/2 & 0 & 1/2 & 0 \\ 0 & 0 & -1/2 & 0 & 1/2 \end{bmatrix}, \tag{32}$$

$$\mathbf{N}_T^{-1} = \begin{bmatrix} 1 & 0 & 0 & 0 & 0 \\ u_x & 1 & 0 & 0 & 0 \\ u_y & 0 & 1 & 0 & 0 \\ u_x^2 & 2u_x & 0 & 1 & 0 \\ u_y^2 & 0 & 2u_y & 0 & 1 \end{bmatrix}. \tag{33}$$

According to Eqs. (17) and (22), we can obtain

$$\left| \Gamma_i^{T,eq} \right\rangle = \mathbf{N}_T^{-1} \left| \tilde{\Gamma}_i^{T,eq} \right\rangle = [T, Tu_x, Tu_y, T(c_T^2 + u_x^2), T(c_T^2 + u_y^2)]^\top. \tag{34}$$

The collision step in Eq. (19) and streaming step in Eq. (24) and can be integrated into one step as,

$$g_i(\mathbf{x} + \mathbf{e}_i \Delta t, t + \Delta t) - g_i(\mathbf{x}, t) = -\mathbf{M}_T^{-1} \mathbf{N}_T^{-1} \mathbf{S}_T \mathbf{N}_T \mathbf{M}_T \left| g_i - g_i^{eq} \right\rangle. \tag{35}$$

According to the Chapman-Enskog expansion, the following multiscale expansions are usually introduced,

$$g_i(\mathbf{x} + \mathbf{e}_i \Delta t, t + \Delta t) = \sum_{i=0}^{\infty} \frac{\varepsilon^n}{n!} (\partial_t + \mathbf{e}_i \cdot \nabla)^n g_i(\mathbf{x}, t), \tag{36a}$$

$$g_i = g_i^{(0)} + \varepsilon g_i^{(1)} + \varepsilon^2 g_i^{(2)} + \ldots, \quad \partial_t = \varepsilon \partial_{t1} + \varepsilon^2 \partial_{t2}, \quad \nabla = \varepsilon \nabla_i, \tag{36b}$$

where ε is the expansion parameter. Using these expansions, the D2Q5 CLBM in Eq. (35) can be written in the consecutive orders of ε,

$$O(\varepsilon^0) : g_i^{(0)} = g_i^{eq}, \tag{37a}$$

$$O(\varepsilon^1) : (\partial_{t1} + \mathbf{e}_i \cdot \nabla_1) g_i^{(0)} = -\frac{1}{\Delta t} \mathbf{M}_T^{-1} \mathbf{N}_T^{-1} \mathbf{S}_T \mathbf{N}_T \mathbf{M}_T \left| g_i^{(1)} \right\rangle, \tag{37b}$$

$$O(\varepsilon^2): \partial_{t2}g_i^{(0)} + (\partial_{t1} + \mathbf{e}_i \cdot \nabla_1)g_i^{(1)} + \frac{\Delta t}{2}(\partial_{t1} + \mathbf{e}_i \cdot \nabla_1)^2 g_i^{(0)}$$

$$= -\frac{1}{\Delta t}\mathbf{M}_T^{-1}\mathbf{N}_T^{-1}\mathbf{S}_T\mathbf{N}_T\mathbf{M}_T\big|g_i^{(2)}\big\rangle. \tag{37c}$$

If we multiply the matrix $\mathbf{M}_T$ on both sides of Eq. (37), the corresponding equations in the raw-moment space can be rewritten as,

$$O(\varepsilon^0): \Gamma_i^{T,(0)} = \Gamma_i^{T,eq}, \tag{38a}$$

$$O(\varepsilon^1): (\mathbf{I}\partial_{t1} + \mathbf{E}_x\partial_{x1} + \mathbf{E}_y\partial_{y1})\Gamma_i^{T,(0)} = -\frac{1}{\Delta t}\mathbf{N}_T^{-1}\mathbf{S}_T\mathbf{N}_T\Gamma_i^{T,(1)}, \tag{38b}$$

$$O(\varepsilon^2): \partial_{t2}\Gamma_i^{T,(0)} + (\mathbf{I}\partial_{t1} + \mathbf{E}_x\partial_{x1} + \mathbf{E}_y\partial_{y1})\left(\mathbf{I} - \frac{1}{2}\mathbf{N}_T^{-1}\mathbf{S}_T\mathbf{N}_T\right)$$

$$\Gamma_i^{T,(1)} = -\frac{1}{\Delta t}\mathbf{N}_T^{-1}\mathbf{S}_T\mathbf{N}_T\Gamma_i^{T,(2)}, \tag{38c}$$

where $\mathbf{E}_i = \mathbf{M}_T[diag(e_{0i}, e_{1,i}, \ldots, e_{4i})]\mathbf{M}_T^{-1}(i = x, y)$ can be written explicitly as

$$\mathbf{E}_x = \begin{bmatrix} 0 & 1 & 0 & 0 & 0 \\ 0 & 0 & 0 & 1 & 0 \\ 0 & 0 & 0 & 0 & 0 \\ 0 & 1 & 0 & 0 & 0 \\ 0 & 0 & 0 & 0 & 0 \end{bmatrix}, \tag{39a}$$

$$\mathbf{E}_y = \begin{bmatrix} 0 & 0 & 1 & 0 & 0 \\ 0 & 0 & 0 & 0 & 0 \\ 0 & 0 & 0 & 0 & 1 \\ 0 & 0 & 0 & 0 & 0 \\ 0 & 0 & 1 & 0 & 0 \end{bmatrix}. \tag{39b}$$

Writing out the equations for the conserved raw moment Γ_0^T, the following equations can be obtained,

$$O(\varepsilon^0): \Gamma_0^{T,(0)} = \Gamma_0^{T,eq}, \tag{40a}$$

$$O(\varepsilon^1): \partial_{t1}\Gamma_0^{T,(0)} + \partial_{x1}\Gamma_1^{T,(0)} + \partial_{y1}\Gamma_2^{T,(0)} = -\frac{\lambda_0}{\Delta t}\Gamma_0^{T,(1)}, \tag{40b}$$

$$O(\varepsilon^2): \partial_{t2}\Gamma_0^{T,(0)} + \partial_{t1}\left[\left(1 - \frac{\lambda_0}{2}\right)\Gamma_0^{T,(1)}\right] + \partial_{x1}\left[\left(1 - \frac{\lambda_1}{2}\right)\Gamma_1^{T,(1)}\right]$$

$$+ \partial_{y1}\left[\left(1 - \frac{\lambda_1}{2}\right)\Gamma_2^{T,(1)}\right]$$

$$= -\frac{\lambda_0}{\Delta t}\Gamma_0^{T,(2)}. \tag{40c}$$

According to Eq. (40a), we have $\Gamma_0^{T,(n)} = 0(n > 0)$. From Eq. (38b), we can get,

$$\Gamma_1^{T,(1)} = -\frac{\Delta t}{\lambda_1}\left[\partial_{t1}(Tu_x) + \partial_{x1}(Tc_T^2 + Tu_x^2)\right], \tag{41a}$$

$$\Gamma_2^{T,(1)} = -\frac{\Delta t}{\lambda_1}\left[\partial_{t1}(Tu_y) + \partial_{y1}(Tc_T^2 + Tu_y^2)\right]. \tag{41b}$$

Substituting Eqs. (41) into Eq. (40c), we can get

$$O(\varepsilon^2): \partial_{t2}T - \nabla_1\left[\Delta t\begin{pmatrix} 1/\lambda_1 - 0.5 & 0 \\ 0 & 1/\lambda_1 - 0.5 \end{pmatrix}\begin{pmatrix} \partial_{t1}(Tu_x) + \partial_{x1}(Tc_T^2 + Tu_x^2) \\ \partial_{t1}(Tu_y) + \partial_{y1}(Tc_T^2 + Tu_y^2) \end{pmatrix}\right] = 0. \tag{42}$$

The term $\partial_{t1}(Tu_x)$ can be rewritten as,

$$\partial_{t1}(Tu_x) = u_x\partial_{t1}(T) + T\partial_{t1}(u_x). \tag{43}$$

Combining Eq. (40b) with the incompressible N-S equation, it can be expressed as

$$\partial_{t1}(Tu_x) = -u_x\left[\partial_{x1}(Tu_x) + \partial_{y1}(Tu_y)\right] - T\left[u_x\partial_{x1}(u_x) + u_y\partial_{y1}(u_x) + \partial_{x1}(p)/\rho_0 - F_{x1}\right]$$

$$= -\partial_{x1}(Tu_x^2) - \partial_{y1}(Tu_xu_y) - T\partial_{x1}(p)/\rho_0 + TF_{x1}, \tag{44}$$

and similar expression can be given for $\partial_{t1}(Tu_y)$. It should be noted that the above expressions for $\partial_{t1}(Tu_x)$ and $\partial_{t1}(Tu_y)$ also apply to many other thermal LBMs [32,35,41]. The four terms on the right side of Eq. (44) can be discussed separately. Firstly, in single-phase flows, numerical errors by the last term are often negligible [42]. Then, as is known, $\delta p = c_s^2\delta\rho$, thus the third term is also negligible in the low-Mach limit. Specifically, in all the simulations at $Ma = 0.3$ in Section 3.3, the measured $\delta\rho$ is always less than 0.05. The first two terms are the sources of non-Galilean artifact. Compared to the methods in [32,35,41], the linear terms can be restored in the present method due to the choice of raw moment equilibria in Eq. (34). After discarding the last two terms and combining Eqs. (44), (42) and (40b), we can obtain

$$\partial_t T + \mathbf{u} \cdot \nabla T = \nabla \cdot (\alpha\nabla T) - \alpha/c_T^2\left[\partial_{xy}(2Tu_xu_y)\right], \tag{45}$$

where the thermal diffusion coefficient, $\alpha = (1/\lambda_1 - 0.5)c_T^2\Delta t$, is assumed to be spatially independent. Analogously, for the methods in [32,35,41], we can obtain

$$\partial_t T + \mathbf{u} \cdot \nabla T = \nabla \cdot (\alpha\nabla T) - \alpha/c_T^2\left[\partial_{xy}(2Tu_xu_y) + \partial_{xx}(Tu_x^2) + \partial_{yy}(Tu_y^2)\right]. \tag{46}$$

As can be seen, the error terms introduced by the present method are less than those by the methods in [32,35,41]. By choosing a larger c_T, the errors terms can be further decreased to some extent. Another interesting argument is that at least half of the errors in [32,35,41] can be removed in the present method, under the assumption of isotropic velocity gradient, due to the fact $u_x^2 + u_y^2 \geqslant 2u_xu_y$. To eliminate the mixed derivative terms, additional correction terms [42] or the D2Q9 lattice can be adopted. In general, the convection-diffusion equation for the temperature field can be recovered by the present D2Q5 CLBM in the low-Mach limit.

Appendix B. Comparison between the present CLBM and the stand BGK-LBM

The 2D lid-driven cavity flow is simulated to fully exploit the stability property of the algorithm. The top wall of a square cavity moves along x direction with a constant velocity $u_0 = 0.1$, while the other walls are fixed. The Reynolds number is defined as $Re = u_0L/\nu$, where L is the cavity length (height). By choosing $L = 80$, a series of numerical cases are carried out using the present D2Q9 CLBM and the standard BGK-LBM [1]. The standard half-way bounce-back scheme is used for all the walls, and the tunable relaxation parameters in CLBM are set to be 1.0. As can be seen in Figs. 10 and 11, unphysical numerical oscillations occur at $Re = 800$ for the standard BGK-LBM, while the density field and velocity field are still smooth at $Re = 2800$ for the present CLBM.
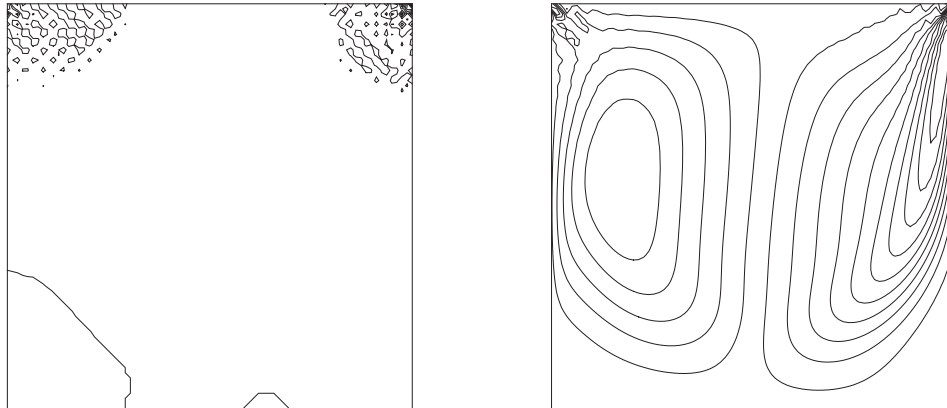
Fig. 10. Contour lines for density (left) and vertical velocity component (right) at *Re* = 800 by standard BGK-LBM. A total of 15 equally divided contours, between the minimum and the maximum, are plotted.
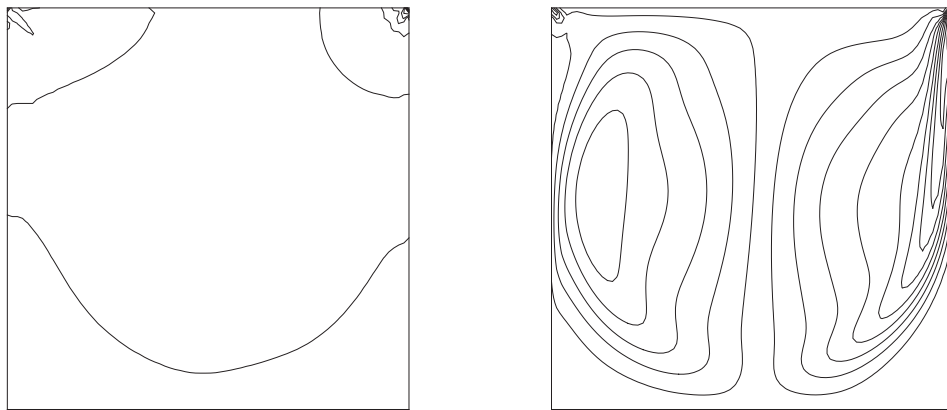

Fig. 11. Contour lines for density (left) and vertical velocity component (right) at *Re* = 2800 by CLBM. A total of 15 equally divided contours, between the minimum and the maximum, are plotted.

References

[1] Y. Qian, D. d'Humières, P. Lallemand, Lattice bgk models for Navier-Stokes equation, EPL (Europhys. Lett.) 17 (6) (1992) 479.

[2] Y.-H. Qian, S. Succi, S. Orszag, Recent advances in lattice Boltzmann computing, Annu. Rev. Comput. Phys. 3 (1995) 195–242.

[3] S. Gong, P. Cheng, A lattice Boltzmann method for simulation of liquid–vapor phase-change heat transfer, Int. J. Heat Mass Transfer 55 (17–18) (2012) 4923–4927.

[4] Q. Li, Q.J. Kang, M.M. Francois, Y.L. He, K.H. Luo, Lattice Boltzmann modeling of boiling heat transfer: the boiling curve and the effects of wettability, Int. J. Heat Mass Transfer 85 (2015) 787–796.

[5] Q. Li, K.H. Luo, Q. Kang, Y. He, Q. Chen, Q. Liu, Lattice Boltzmann methods for multiphase flow and phase-change heat transfer, Prog. Energy Combust. Sci. 52 (2016) 62–105.

[6] S. Chen, B. Yang, K.H. Luo, X. Xiong, C. Zheng, Double diffusion natural convection in a square cavity filled with nanofluid, Int. J. Heat Mass Transfer 95 (2016) 1070–1083.

[7] C. Lin, K.H. Luo, L. Fei, S. Succi, A multi-component discrete Boltzmann model for nonequilibrium reactive flows, Sci. Rep. 7 (1) (2017) 14580.

[8] I. Ginzburg, D. d'Humières, Multireflection boundary conditions for lattice Boltzmann models, Phys. Rev. E 68 (6) (2003) 066614.

[9] C. Pan, L.-S. Luo, C.T. Miller, An evaluation of lattice Boltzmann schemes for porous medium flow simulation, Comput. Fluids 35 (8) (2006) 898–909.

[10] D. d'Humieres, Generalized lattice-Boltzmann equations, Raref. Gas Dyn. – Theory Simul. (1994) 450–458.

[11] P. Lallemand, L.-S. Luo, Theory of the lattice Boltzmann method: dispersion, dissipation, isotropy, Galilean invariance, and stability, Phys. Rev. E 61 (6) (2000) 6546.

[12] D. d'Humières, Multiple–relaxation–time lattice Boltzmann models in three dimensions, Philosoph. Trans. Roy. Soc. Lond. A: Math., Phys. Eng. Sci. 360 (1792) (2002) 437–451.

[13] H. Chen, P. Gopalakrishnan, R. Zhang, Recovery of Galilean invariance in thermal lattice Boltzmann models for arbitrary Prandtl number, Int. J. Mod. Phys. C 25 (10) (2014) 1450046.

[14] M. Geier, A. Greiner, J.G. Korvink, Cascaded digital lattice Boltzmann automata for high Reynolds number flow, Phys. Rev. E 73 (6) (2006) 066705.

[15] Y. Ning, K.N. Premnath, D.V. Patil, Numerical study of the properties of the central moment lattice Boltzmann method, Int. J. Numer. Methods Fluids 82 (2) (2016) 59–90.

[16] A. De Rosis, Central-moments-based lattice Boltzmann schemes with force-enriched equilibria, EPL (Europhys. Lett.) 117 (3) (2017) 34003.

[17] A. De Rosis, Nonorthogonal central-moments-based lattice Boltzmann scheme in three dimensions, Phys. Rev. E 95 (1) (2017) 013310.

[18] D. Lycett-Brown, K.H. Luo, Multiphase cascaded lattice Boltzmann method, Comput. Math. Appl. 67 (2) (2014) 350–362.

[19] D. Lycett-Brown, K.H. Luo, R. Liu, P. Lv, Binary droplet collision simulations by a multiphase cascaded lattice Boltzmann method, Phys. Fluids 26 (2) (2014) 023303.

[20] H. Chen, C. Teixeira, K. Molvig, Digital physics approach to computational fluid dynamics: some basic theoretical features, Int. J. Mod. Phys. C 8 (04) (1997) 675–684.

[21] M. Geier, A. Pasquali, M. Schönherr, Parametrization of the cumulant lattice Boltzmann method for fourth order accurate diffusion part i: derivation and validation, J. Comput. Phys. 348 (2017) 862–888.

[22] D. Lycett-Brown, K.H. Luo, Cascaded lattice Boltzmann method with improved forcing scheme for large-density-ratio multiphase flow at high Reynolds and Weber numbers, Phys. Rev. E 94 (5) (2016) 053313.

[23] A. De Rosis, A central moments-based lattice Boltzmann scheme for shallow water equations, Comput. Methods Appl. Mech. Eng. 319 (2017) 379–392.

[24] F. Hajabdollahi, K.N. Premnath, Improving the low Mach number steady state convergence of the cascaded lattice Boltzmann method by preconditioning, Comput. Math. Appl. (2017), https://doi.org/10.1016/j.camwa.2016.12.034.

[25] K.N. Premnath, S. Banerjee, Incorporating forcing terms in cascaded lattice Boltzmann approach by method of central moments, Phys. Rev. E 80 (3) (2009) 036702.

[26] A. De Rosis, Alternative formulation to incorporate forcing terms in a lattice Boltzmann scheme with central moments, Phys. Rev. E 95 (2) (2017) 023311.

[27] L. Fei, K.H. Luo, Consistent forcing scheme in the cascaded lattice Boltzmann method, Phys. Rev. E 96 (2017) 053307.

[28] L. Fei, K.H. Luo, Thermal cascaded lattice Boltzmann method. Available from: arXiv preprint <1610.07114>.

[29] Z. Guo, B. Shi, C. Zheng, A coupled lattice bgk model for the Boussinesq equations, Int. J Numer. Methods Fluids 39 (4) (2002) 325–342.

[30] Z. Guo, C. Zheng, B. Shi, T. Zhao, Thermal lattice Boltzmann equation for low Mach number flows: decoupling model, Phys. Rev. E 75 (3) (2007) 036704.

[31] S. Gong, P. Cheng, Lattice Boltzmann simulation of periodic bubble nucleation, growth and departure from a heated surface in pool boiling, Int. J. Heat Mass Transfer 64 (3) (2013) 122–132.

[32] Q. Liu, Y.-L. He, D. Li, Q. Li, Non-orthogonal multiple-relaxation-time lattice Boltzmann method for incompressible thermal flows, Int. J. Heat Mass Transfer 102 (2016) 1334–1344.

[33] N. Shah, P. Dhar, S.K. Chinige, M. Geier, A. Pattamatta, Cascaded collision lattice Boltzmann model (clbm) for simulating fluid and heat transport in porous media, Numer. Heat Transfer, Part B: Fundam. 72 (3) (2017) 211–232.

[34] C.S. Kumar, S. Mohankumar, M. Geier, A. Pattamatta, Numerical investigations on convective heat transfer enhancement in jet impingement due to the presence of porous media using cascaded lattice Boltzmann method, Int. J. Therm. Sci. 122 (2017) 201–217.

[35] K.V. Sharma, R. Straka, F.W. Tavares, New cascaded thermal lattice Boltzmann method for simulations of advection-diffusion and convective heat transfer, Int. J. Therm. Sci. 118 (2017) 259–277.

[36] P. Asinari, Generalized local equilibrium in the cascaded lattice Boltzmann method, Phys. Rev. E 78 (2) (2008) 016701.

[37] X. He, X. Shan, G.D. Doolen, Discrete Boltzmann equation model for nonideal gases, Phys. Rev. E 57 (1) (1998) R13–R16.

[38] X. He, L.-S. Luo, Lattice Boltzmann model for the incompressible Navier–Stokes equation, J. Stat. Phys. 88 (3) (1997) 927–944.

[39] Q. Zou, X. He, On pressure and velocity boundary conditions for the lattice Boltzmann bgk model, Phys. Fluids 9 (6) (1997) 1591–1598.

[40] H. Yoshida, M. Nagaoka, Multiple-relaxation-time lattice Boltzmann model for the convection and anisotropic diffusion equation, J. Comput. Phys. 229 (20) (2010) 7774–7795.

[41] S. Cui, N. Hong, B. Shi, Z. Chai, Discrete effect on the halfway bounce-back boundary condition of multiple-relaxation-time lattice Boltzmann model for convection-diffusion equations, Phys. Rev. E 93 (4) (2016) 043311.

[42] Q. Li, K.H. Luo, Effect of the forcing term in the pseudopotential lattice Boltzmann modeling of thermal flows, Phys. Rev. E 89 (5) (2014) 053022.

[43] D.R. Noble, S. Chen, J.G. Georgiadis, R.O. Buckius, A consistent hydrodynamic boundary condition for the lattice Boltzmann method, Phys. Fluids 7 (1) (1995) 203–209.

[44] R. Clever, F. Busse, Transition to time-dependent convection, J. Fluid Mech. 65 (04) (1974) 625–645.

[45] N.I. Prasianakis, I.V. Karlin, Lattice Boltzmann method for thermal flow simulation on standard lattices, Phys. Rev. E 76 (1) (2007) 016702.